ACS Sustainable Chemistry & Engineering

pubs.acs.org/journal/ascecg

Research Article

Structure and Intrinsic Mechanical Properties of Nanocrystalline Calcium Silicate Hydrate

Jiaqi Li,* Wenxin Zhang, and Paulo J. M. Monteiro

Cite This: *ACS Sustainable Chem. Eng.* 2020, 8, 12453−12461

Read Online

ACCESS | Metrics & More | Article Recommendations | Supporting Information

ABSTRACT: Nanocrystalline calcium silicate hydrate (C−S−H) is the binding phase of many low-CO_2 cements. Understanding its structure−mechanical properties relationship is critical in designing sustainable concrete. For the first time, a similar basal spacing (only 0.17 Å variation) of C−S−Hs at Ca/Si ratios of 0.8−1.5 is prepared via coprecipitation. The C−S−H nanostructure is determined using X-ray absorption spectroscopy, and the intrinsic nanomechanical properties of C−S−H at various Ca/Si are measured using high-pressure X-ray diffraction. For the first time, the influence of basal spacing on the nanomechanical properties is eliminated. At similar basal spacing, the *ab*-planar incompressibility remains independent of Ca/Si and silicate chain length, while the *c*-axis incompressibility is governed by the interlayer density (i.e., interlayer Ca content). The bulk modulus of C−S−H is governed by the interlayer density—more interlayer Ca yields higher bulk modulus at comparable basal spacings. Our results show that coprecipitated C−S−Hs at higher Ca/Si have higher mechanical properties. The results have implications in designing green cement/concrete using bottom-up approaches by providing property inputs for multiscale simulation and references for validating computational methods/parameters.

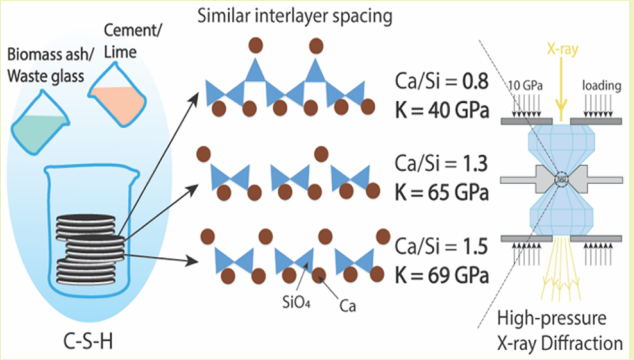

KEYWORDS: *Sustainable cement, Green concrete, C−S−H, Basal spacing, Nanomechanical properties, XANES, High-pressure XRD, Interlayer density*

INTRODUCTION

Portland cement (PC)-based concrete is the most used construction material. The global annual production of PC is over 4 Gt, which contributes to ∼9% of global anthropogenic CO_2 emissions.[1] Lowering the CO_2 emission of cement manufacture and pursuing sustainable (alternative) cements are of great interest to both the industry and academia.[2]

Partial substitution of PC with industrial byproducts (e.g., fly ash from coal-fired power plants and ground-granulated blast-furnace slag (GGBFS) from ironmaking) with high glassy content of (alumino)silicate has shown decades of success in lowering the CO_2 emission of concrete production and improving the mechanical properties and durability of concrete.[3,4] Other green alternatives to PC have also been extensively studied. For example, alkali-activated materials (e.g., alkali-activated GGBFS and coal fly ash)[5,6] have shown relatively low associated CO_2 emissions and comparable mechanical properties relative to PC-based materials.[7,8] However, the available high-quality coal fly ash (300 Mt/year) is insufficient for tremendous cement demand, and the use of low-quality fly ash is subjected to the limitations on carbon content, toxic elements, and reactivity.[9,10] An exacerbated shortage of coal fly ash has been observed due to the threatened supply chain caused by retirement of coal-fired power plants and the pursuit of renewable and sustainable energy. The supply of GGBFS is also limited (∼330 Mt/year)[9] relative to the massive demand of PC. Air-cooled blast-furnace slag in new ironmaking plants is not pozzolanically reactive, and thus not suitable for cement substitution.[9]

The pursuit of alternative amorphous (alumino)silicate sources can compensate for the global shortage of coal fly ash and GGBFS.[11] Natural resources, e.g., volcanic ash[12] and diatomite,[13] have shown great performance as cement substitutes. There is also a burgeoning interest in the use of renewable sources (or other wastes) of amorphous silica in PC substitution. This wide variety of sources includes agricultural waste ashes,[14] biomass residues (e.g., rice husk ash),[15] and waste glass sludge.[16] The substitution of PC with these sources has shown great improvement in strengths and/or a reduction of environmental impacts during concrete production. Additionally, these alternative (alumino)silicate sources can be

Received: April 30, 2020
Revised: July 24, 2020
Published: July 28, 2020

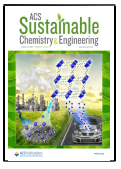

blended with lime for casting sustainable masonry or other construction materials.[17]

When high-volume amorphous silicate is used to substitute PC or to blend with lime, the primary binding phase of these systems is nanocrystalline calcium silicate hydrate (C−S−H).[18] In addition, this C−S−H phase is similar to the binding phase of alkali-activated high Ca coal fly ash or GGBFS.[19] C−S−H typically has a wide range of molar Ca/Si ratio at 0.67−1.65[20] and a structural ordering at 3−5 nm.[21] The gel pores between the nanocrystals are water- or gas-filled.[22] The nanostructure of C−S−H has been proposed as a defected tobermorite[23] with a layer-stacked structure of basal layers (CaO_7 sheet flanked between silicate tetrahedral chains)[24] and a hydrated interlayer[25,26] (see Figure 1).

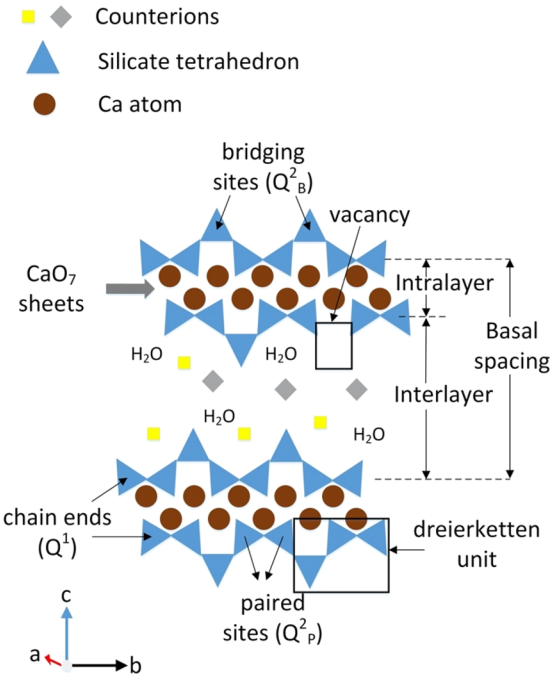

Figure 1. Schematic of the C−S−H structure from a defected tobermorite. C−S−Hs are typically nanocrystalline while natural tobermorite has infinite silicate chains.

The mechanical properties of cement-based materials are of great significance for buildings and infrastructures. Mechanical properties of C−S−H have been measured mainly at the submicron scale using nanoindentation,[27] which cannot preclude the influences of gel pores and packing density.[28] A recent study using high-pressure X-ray diffraction (HP-XRD) determined the nanomechanical properties of C−S−H at unit-cell scale (i.e., a pore-free scale).[29,30] These C−S−Hs were synthesized by the CaO−SiO_2 reaction; thus, the pH and Ca/Si ratio of C−S−Hs are positively correlated.[31] HP-XRD results have shown that the incompressibility of the CaO−SiO_2 reacted C−S−H along the *c*-axis is Ca/Si-dependent and is influenced by its interlayer density−different basal spacings and interlayer Ca contents. The basal spacing of C−S−H synthesized by the CaO−SiO_2 reaction increases as the bulk Ca/Si ratio decreases. The influences of two variables (the basal spacing and interlayer Ca content) on the nanomechanical properties of the CaO−SiO_2 reacted C−S−H have not yet been decoupled in the previous HP-XRD study.[30] Moreover, many amorphous silicates (e.g., biomass ash or shale ash) are typically alkali-rich, meaning that the pH and Ca/Si of C−S−H can be negatively correlated. The scenarios with the use of alkali-rich amorphous silicate can be mimicked by a coprecipitation method from Ca salts (e.g., $Ca(NO_3)_2{\cdot}4H_2O$) and water−glass. A recent study of coprecipitated C−S−Hs shows a low variation, ∼1 Å, in basal spacing at Ca/Si ratios of 0.64−1.25.[32] This fact indicates that comparable basal spacings of C−S−H at various Ca/Si ratios may be achievable. Further investigations may allow us to study the sole influence of Ca content on the nanomechanical properties of C−S−H by eliminating the effect of different basal spacings.

In this study, phase-pure nanocrystalline C−S−Hs with various Ca/Si ratios were synthesized using the coprecipitation method to mimic the influence of pH from amorphous alkali-rich silicate (e.g., biomass ash) on the structure and nanomechanical properties of C−S−H. The nanomechanical properties of C−S−Hs were measured using HP-XRD. The influences of the basal spacing and Ca content on the nanomechanical properties of C−S−H were, for the first time, decoupled. The local Ca and Si environments of C−S−H were probed using X-ray absorption near edge fine structure (XANES) spectroscopy at the Ca $L_{2,3}$-edge and Si *K*-edge, respectively. The study has great implications in optimization of the mechanical properties of cement/concrete with a high volume of Si-rich byproducts and sustainable lime-biomass construction materials using bottom-up approaches. The experimental results obtained in this study can validate computational studies of nanomechanical properties of C−S−H using molecular dynamics and/or density functional theory[33,34] and can provide valuable evidence for optimizing the computational methods and parameters (e.g., Lennard-Jones potential) in the studies of C−S−H.

EXPERIMENTAL SECTION

Materials. The coprecipitated C−S−Hs were synthesized at initial bulk Ca/Si ratios of 0.8, 1.3, and 1.5. Stoichiometric amounts of $Ca(NO_3)_2{\cdot}4H_2O$ (99+%, Fisher) and $Na_2SiO_3{\cdot}9H_2O$ (99+%, Fisher) were mixed with deionized water in 500 mL HDPE bottles in a N_2-filled glovebox. The bottles were stirred at 60 rpm and cured for 7 days at 25 °C. Subsequently, the samples were vacuum filtered using 450 nm nylon filters under N_2 protection for 45 min with a vacuum pump (flow rate 37 L/min, Millipore Sigma). 95 vol % isopropanol solution was used to rinse the gel-like slurry. ∼2 g of gel was vacuum-dried for 7 days at 25 °C using the vacuum pump (flow rate 37 L/min, Millipore Sigma) with the presence of 10 g NaOH pellets (97+%, Fisher) in a 10.5 L desiccator (24/29 standard taper stopcock, Pyrex) to avoid carbonation. This drying protocol was modified from the vacuum drying method used in our previous study of C−S−H.[35] The drying in the present study may be slightly harsher than our previous study[35] for avoiding carbonation due to the higher alkalinity of the coprecipitated C−S−H in the present study, but not harsher than other conventional drying methods, e.g., freeze-drying[36] and drying at 40−105 °C,[37,38] used in C−S−H syntheses. Richardson[20] summarized the influence of different drying protocols on the influences of water content in C−S−Hs. Vacuum drying at room temperature is not aggressive for C−S−H. Excessive drying typically results in the reductions of intensity of the basal peak, i.e., (002) peak, and the basal spacing of C−S−H.[38] Thus, excessive drying methods (e.g., freeze-drying and drying at 105 °C) were avoided in this study. The dried samples were vacuum-sealed until analysis. The final Ca/Si ratios of the samples are listed in Table 1.

XANES. The XANES spectra of the C−S−H samples at the Ca $L_{2,3}$-edge and Si *K*-edge were measured using scanning transmission X-ray microscopy at the beamlines 5.3.2.2 and 5.3.2.1, respectively, at the Advanced Light Source (ALS) of Lawrence Berkeley National Laboratory. The samples were cast on SiN windows (100 nm thick).

https://dx.doi.org/10.1021/acssuschemeng.0c03230
ACS Sustainable Chem. Eng. 2020, 8, 12453−12461

Table 1. Compositions and pH of the Coprecipitated C−S−Hs

initial Ca/Si	final mean Ca/Si[a]	pH of solution
0.8	0.84	12.83
1.3	1.27	11.83
1.5	1.43	11.54

[a]Measured by energy dispersive X-ray spectroscopy. For more details about the pH measurement and composition measurement of C−S−H, see the Supporting Information. Na content is trace.

For the XANES measurement at the Ca $L_{2,3}$-edge, the samples were mounted into a dry He-filled chamber at 1/3 atm, while samples measured at the Si *K*-edge were mounted into a vacuum chamber (200 mTorr). The XANES spectra at the Ca $L_{2,3}$-edge (345−356 eV) were collected in line-scan mode at an energy resolution of 0.1 eV with a dwell time of 10 ms; XANES spectra at the Si *K*-edge (1840−1880 eV) were measured in line-scan mode with an energy resolution of 0.3 eV and a dwell time of 50 ms. The XANES spectra were processed using Axis2000.

High-Pressure XRD. The HP-XRD experiment was conducted at the beamline 12.2.2 at the ALS. A monochromatic X-ray beam at energy of 20 keV (wavelength 0.6133 Å) was used. The sample-to-detector distance (220 mm) and beam wavelength were calibrated using fine CeO_2 powder. Each sample was loaded, with at least one ruby (Cr^{3+}-doped Al_2O_3) sphere as the hydrostatic pressure gauge, into a chamber (100 μm diameter and 100 μm thickness) of a stainless-steel gasket. The chamber was immersed by methanol/ethanol solution (4:1 v/v) as a pressure-transmitting medium and sealed by a pair of diamond anvils in a BX90 diamond anvil cell. The hydrostatic pressure of all samples at each loading was determined using the ruby fluorescence method.[39] Each diffraction pattern was recorded on a two-dimensional Pilatus image plate with an exposure time of 420 s at 23 °C. The data were processed using XFIT, Dioptas, and Celref with Merlino's B11m tobermorite structure.[40]

The Biot strain of a unit cell of the C−S−H is defined in eq 1:

$$\text{Biot strain} = \frac{l - l_0}{l_0} \tag{1}$$

Here, l and l_0 are the lattice parameters at the measured hydrostatic pressure and ambient pressure, respectively.

The third-order Birch−Murnaghan equation of state (eq 2) describes the relationship between the pressure-induced volumetric change of a unit cell and its bulk modulus at the ambient-pressure.

$$P = \frac{3}{2}K_0[(1-\varepsilon_V)^{-7/3} - (1-\varepsilon_V)^{-5/3}]\left[1 + \frac{3}{4}(K'_0 - 4)(\varepsilon_V{}^{-2/3} - 1)\right] \tag{2}$$

Here, P is the measured hydrostatic pressure in the chamber (GPa), ε_V is the volumetric strain of a C−S−H unit cell, K_0 is the bulk modulus at ambient pressure (GPa), and K'_0 is the pressure derivative of K_0. K'_0 is assumed to be 4 in the second-order Birch−Murnaghan equation of state (see eq 3). The second-order Birch−Murnaghan equation of state is applied to calculate the K_0 of cement-related (nano)crystalline phases because (1) K'_0 for many cement-related phases often is approximately 4, and (2) the use of the third-order Birch−Murnaghan equation of state in a low range of applied hydrostatic pressure (typically below 10 GPa for cement-related phases) typically results in unreliable calculated K'_0 (i.e., either too small or too large). Higher pressure ranges may result in highly disordered structures, which are difficult for determining the unit cell parameters under pressure.

$$P = \frac{3}{2}K_0[(1-\varepsilon_V)^{-7/3} - (1-\varepsilon_V)^{-5/3}] \tag{3}$$

RESULTS AND DISCUSSION

Ca Coordination. The XANES spectra of the coprecipitated C−S−H at the Ca $L_{2,3}$-edge are shown in Figure 2. The

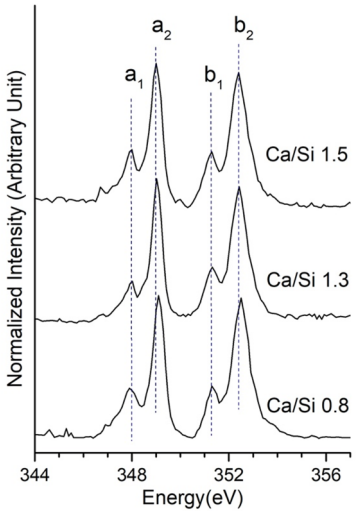

Figure 2. XANES spectra of coprecipitated C−S−Hs with various Ca/Si ratios at the Ca $L_{2,3}$-edge.

spectra represent the electron transition of Ca atoms from $2p^63d^0$ to $2p^53d^1$ configuration. Two major peaks, L_3 ($2p_{3/2}$, a_2 peak) and L_2 ($2p_{1/2}$, b_2 peak), are observed due to the loss of degeneracy of 2p orbitals.[41] a_1 and b_1 minor peaks at the left of each major peak originate from crystal field splitting.[42] The position and number of the minor peaks are related to a certain symmetry of Ca (either octahedral or cubic).[43] The energy difference (splitting energies, $\Delta L_3 = a_2 - a_1$ and $\Delta L_2 = b_2 - b_1$) between the adjacent major and minor peaks depends on the first neighbor of Ca and the distortion degree of the symmetry.[44]

The presence of only two minor peaks (a_1 and b_1) suggests that the Ca−O complex in coprecipitated C−S−H possesses an octahedral-like coordination symmetry.[45] However, the peak intensity of a_1 and b_1 is relatively low, suggesting that this symmetry is highly distorted from a perfect octahedron. This low symmetry is consistent with existing models of C−S−H where the intralayer Ca−O sheet is in 7-fold coordination.[46] The effect of Ca/Si ratio on XANES spectra at the Ca $L_{2,3}$-edge seems insignificant; this is because the major environment of Ca is CaO_7 in the basal layer.

As Ca/Si increases, the major peak (a_2 and b_2) positions slightly shift to a lower energy by 0.1 eV (see Table 2). The lower energy of major peaks at Ca/Si of 1.3 and 1.5 suggests a lower oxidation degree of Ca, i.e., lower average coordination number of Ca, meaning that more 6-fold coordinated interlayer Ca exists at a higher Ca/Si ratio (see Figure 3), consistent with the XANES results of C−S−H synthesized via $CaO-SiO_2$ reaction.[47] The energy difference between each doublet (ΔL_3 and ΔL_2) at Ca/Si of 1.3 and 1.5 is 1.1 eV, which is relatively low, indicating the high distortion of both the Ca−O sheet and the 6-fold coordinated interlayer Ca.[43] Interestingly, ΔL_3 and ΔL_2 of coprecipitated C−S−H at Ca/Si of 0.8 are ~0.1 eV greater than those at higher Ca/Si (i.e., 1.3 and 1.5), suggesting that the interlayer Ca (including Ca^{2+} and $CaOH^+$) is less distorted (more octahedral-like and more symmetric) at Ca/Si of 0.8. In our previous XANES study[47] of C−S−H synthesized via $CaO-SiO_2$ reaction, such differences

https://dx.doi.org/10.1021/acssuschemeng.0c03230
ACS Sustainable Chem. Eng. 2020, 8, 12453−12461

Table 2. Absorption Features in the XANES Spectra of Coprecipitated C−S−H at the Ca $L_{2,3}$-Edge

	energy (eV)					
Ca/Si	a_1	a_2	$\Delta L_3 = a_2 - a_1$	b_1	b_2	$\Delta L_2 = b_2 - b_1$
0.8	347.92	349.1	1.18	351.3	352.5	1.2
1.3	347.98	349.05	1.07	351.32	352.42	1.1
1.5	347.95	349.0	1.05	351.3	352.4	1.1

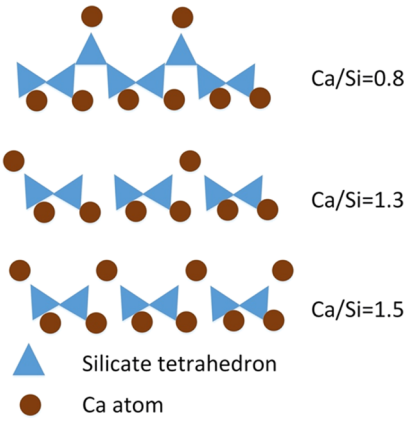

Figure 3. Structure of basal layer of coprecipitated C−S−H at various Ca/Si ratios. The tangling O of paired silicate can be charge-balanced by proton.

in the environment of interlayer Ca at low Ca/Si ratios were not observed. Thus, the high symmetry of interlayer Ca of coprecipitated C−S−H in the present study may be due to the high pH at Ca/Si of 0.8 (contributed by the water glass). Gartner et al.[48] suggested that $CaOH^+$ is dominant in the interlayer when pH of C−S−H is high. Kumar et al. confirmed that hydroxyl groups can charge-balance interlayer Ca, and the C−S−H is stabilized by a strong hydrogen bonding particularly at high pH (>12.5).[49]

Silicate Polymerization. The XANES spectra of coprecipitated C−S−H at the Si *K*-edge are shown in Figure 4. The major peak X (Si *K*-edge) at 1849.0−1850.1 eV correspond to

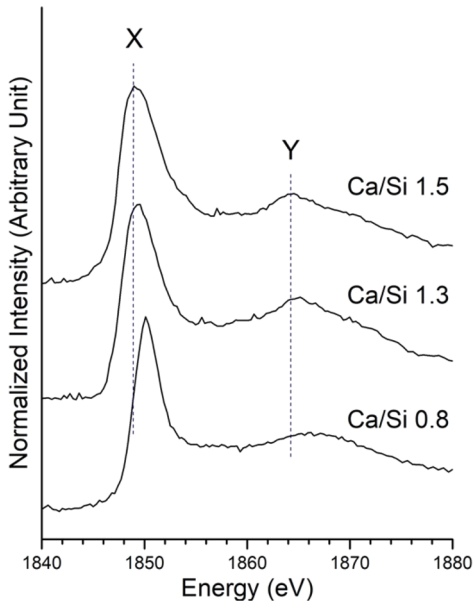

Figure 4. XANES spectra of coprecipitated C−S−H at the Si *K*-edge.

the excitation from 1s to 3p orbital in tetrahedral Si. The minor peaks Y (at ∼1864.6−1867.2 eV) are attributed to the multiscattering effect from more distant shells through photoelectron interaction, and its energy is related to the interatomic distance.[50,51] The peak positions and energy separation between X and Y peaks are listed in Table 3. As

Table 3. Absorption Features in the XANES Spectra of Coprecipitated C−S−H at the Si *K*-Edge

Ca/Si	X (eV)	Y (eV)	Y − X (eV)
0.8	1850.1	1867.2	17.1
1.3	1849.4	1865.3	15.9
1.5	1849.0	1864.6	15.6

the Ca/Si ratio increases, the Si *K*-edges gradually shift to lower energy by 1.1 eV (Figure 5). This energy decrease is caused by the increase in the electron shielding from more Ca^{2+} at the second shell of Si,[52] suggesting a lower silicate polymerization of C−S−H at high Ca/Si. This observation is consistent with our interpretation of the Ca environment and previous work on C−S−H[35] and silicate minerals.[52] The Si *K*-edge peak X broadens at an increased Ca/Si ratio, suggesting reduced long-range ordering of tetrahedral Si.[53] The minor peak Y also shifts to lower energy as the Ca/Si ratio increases, indicating longer Si−O distances.[54,55] In addition, the energy difference between X and Y peaks decreases as Ca/Si increases, also suggesting a lower degree of silicate polymerization[43] at higher Ca/Si.

Nanomechanical Properties. The lattice parameters of coprecipitated C−S−H at various Ca/Si ratios at ambient pressure do not show significant variations (see Table 4). Only ∼0.2 Å difference in basal spacing was observed at Ca/Si ratios of 0.8−1.5. Such a low variation in basal spacing across various Ca/Si can be explained by the existence of interlayer $CaOH^+$ of C−S−H at a Ca/Si ratio of 0.8 and the lack of $CaOH^+$ at higher Ca/Si ratios, as suggested in our XANES results. Another factor that may influence the basal spacing of C−S−H is the drying process. Lower humidity or excessive drying results in the loss of interlayer water of C−S−H, thus considerably reducing the intensity and *d*-spacing of the basal peak (i.e., 002 peak).[38] In the present study, the 002 peak at ambient pressure is apparently sharp, and as described in the Experimental Section, our vacuum drying at 25 °C was not excessive. Thus, it is not likely that the comparable basal spacing of C−S−H across various Ca/Si ratios here was caused by the drying process. Our measured H_2O/Si ratios at various Ca/Si are within the range of common H_2O/Si ratios of C−S−H summarized in a comprehensive data set,[20] confirming that the drying process was not excessive. To our knowledge, comparable basal spacings of C−S−H using different drying protocols in our published studies[29,30,37,56] of $CaO-SiO_2$ reacted C−S−H and in many unpublished studies were not found. Therefore, the comparable basal spacing of coprecipitated C−S−Hs at various Ca/Si is assigned to the strong

https://dx.doi.org/10.1021/acssuschemeng.0c03230
ACS Sustainable Chem. Eng. 2020, 8, 12453−12461

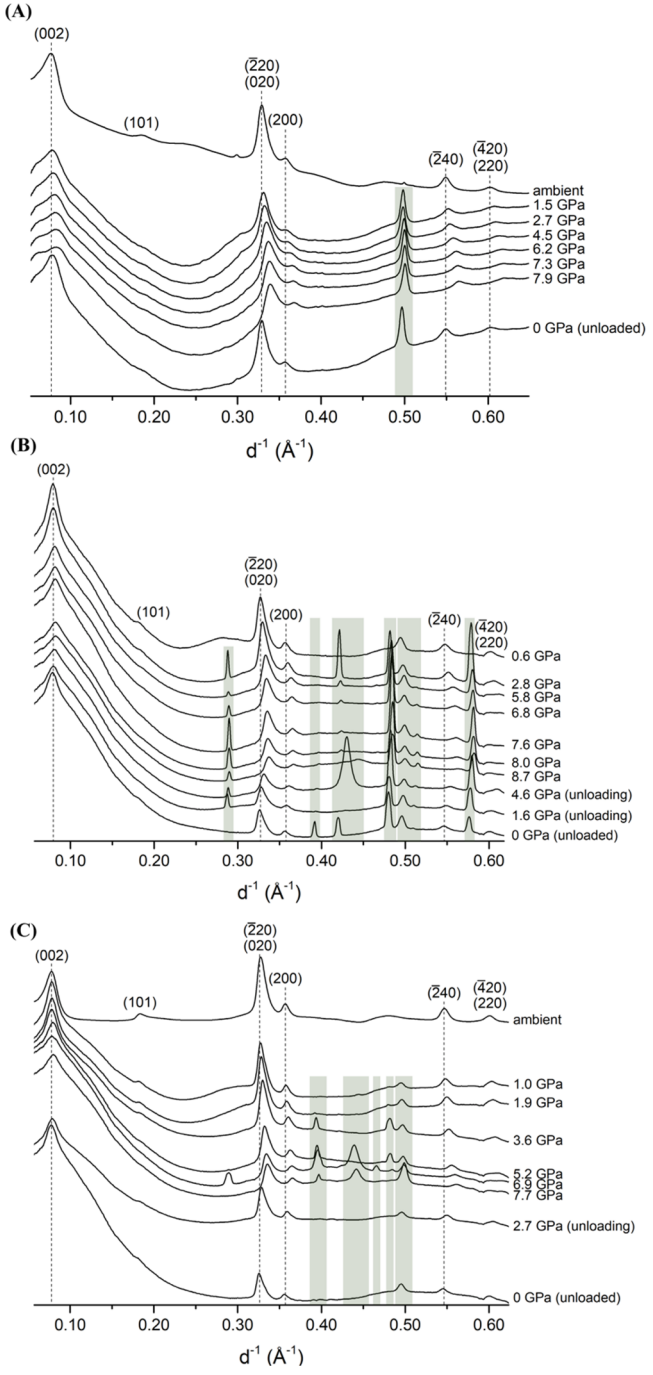

Figure 5. X-ray diffractogram of coprecipitated C−S−H at Ca/Si of (A) 0.8, (B) 1.3, and (C) 1.5. Dashed lines represent the C−S−H peak positions at ambient pressure as reference. Diffraction of gaskets and ruby is masked by green strips. The uncertainty of applied hydrostatic pressure is ∼0.1 GPa.

interlayer $CaOH^+$[49] at low Ca/Si (caused by negative pH-Ca/Si correlation in the coprecipitation method). A low variation in basal spacing, 1 Å, at various Ca/Si ratios (0.64−1.25) was also observed in a study of coprecipitated C−S−H,[32] where the influences of carbonation were not well controlled. (Note that the pH of all samples was kept at 13.) Coprecipitated C−S−Hs with various Ca/Si ratios (1.0−1.5) were also prepared in Hunnicutt et al.,[57] where an apparent variation in basal spacing was not found, and the measured pH was similar to the present study. Future work will systematically investigate the influences of pH and interlayer $CaOH^+$ on the atomistic structure of coprecipitated C−S−H using different characterization techniques.

Table 4. Lattice Parameters and Water Content of Coprecipitated C−S−H at Various Ca/Si Ratios

Ca/Si	a (Å)	b (Å)	c (Å)	γ (deg)	V (Å^3)	basal spacing (Å)	H_2O/Si[a]
0.8	6.693	7.297	25.5	123.1	1039	12.76	1.0
1.3	6.698	7.331	25.4	123.2	1040	12.68	1.5
1.5	6.689	7.341	25.7	123.2	1060	12.85	1.7

[a]Measured by thermogravimetry analysis; for more details, see the method in the Supporting Information.

As applied hydrostatic pressure increases, the diffraction peaks of all coprecipitated C−S−H monotonically shift to the right (see Figure 5), corresponding to shorter interplanar distances. Pressure-induced peak broadening is observed at increased pressure due to decreased structural ordering of C−S−H.[58] This loss of structural ordering at high pressure is very common in HP-XRD studies of cementitious materials.[59,60]

The axial incompressibility (see the slope in Figure 6) of a unit cell is defined by the Biot strain along each axis of a unit cell as a linear function of applied hydrostatic pressure. The incompressibility along the a- and b-axes (see Figure 6A) of coprecipitated C−S−H at Ca/Si of 0.8−1.5 ranges from −1/271 to −1/323 GPa^{-1}, which is similar to the ab-planar incompressibility of tobermorite[61] and CaO−SiO_2 reacted C−S−H.[30] The ab-planar incompressibility is independent of Ca/Si ratios, and thus independent of the degree of silicate polymerization (mean silicate chain length). A previous simulation study[30] suggests that highly polymerized silicate chains (continuous, e.g., Ca/Si = 0.8) deform mainly due to the tilting between bridging tetrahedra and adjacent paired tetrahedra rather than the contraction of Si−O bonds while poorly polymerized chains (discontinuous, e.g., Ca/Si = 1.5) do not significantly contribute to the b-axis deformation.

The Biot strain along the c-axis versus hydrostatic pressure of the coprecipitated C−S−H shows dependence on Ca/Si ratio (see Figure 6B). As Ca/Si increases, the incompressibility (also by linear fitting of the pressure−Biot strain correlation) along the c-axis of C−S−H gradually increases. This positive correlation suggests that the c-axis incompressibility is not dominated by the basal spacing as the basal spacings of all coprecipitated C−S−H in the present study are highly comparable. Instead, the more incompressible c-axis at higher Ca/Si ratio relates to the higher density of the interlayer (i.e., more Ca) at fixed basal spacing. Our recent HP-XRD study of 11 Å double-chain tobermorite with equivalent basal spacing but various Ca content also demonstrates that the c-axis incompressibility is dominated by the density of interlayer (i.e., Ca content) at constant basal spacings.[61]

The measured bulk modulus (K_0) of coprecipitated C−S−H increases at increased Ca/Si ratio (see Figure 7). As the ab-planar incompressibility shows the independence of the Ca/Si ratio, and the c-axis incompressibility shows a positive correlation with the Ca/Si ratio, K_0 (volumetric strain dependent) of C−S−H at various Ca/Si ratios shows a positive relationship with the c-axis incompressibility. Thus, K_0 of C−S−H essentially positively correlates to the c-axis incompressibility. As the basal spacing of coprecipitated C−S−H at various Ca/Si ratios is highly comparable, K_0 here is

https://dx.doi.org/10.1021/acssuschemeng.0c03230
ACS Sustainable Chem. Eng. 2020, 8, 12453−12461

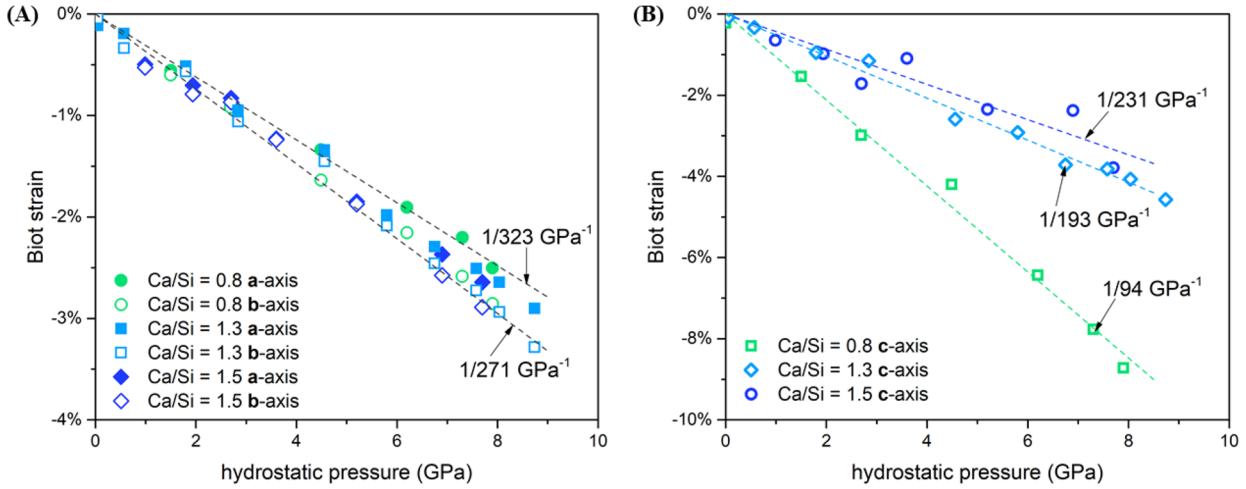

Figure 6. Biot strain of coprecipitated C−S−Hs as a function of applied hydrostatic pressure along (A) the *a*- and *b*-axes; and (B) the *c*-axis. The estimated uncertainty of applied hydrostatic pressure is 0.1 GPa. The uncertainty of the Biot strain is <0.2%. The axial incompressibilities indicated here were obtained by linear fitting.

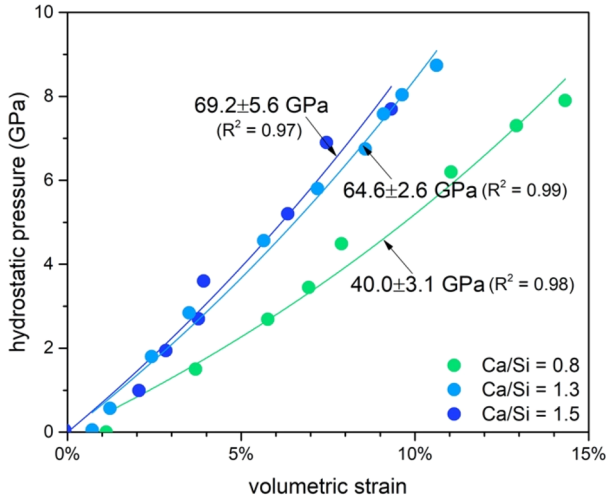

Figure 7. Ambient bulk modulus K_0 of coprecipitated C−S−H by fitting the second-order Birch−Murnaghan equation of state described in the Experimental Section. The estimated uncertainty of applied hydrostatic pressure is 0.1 GPa.

governed by the density of the basal layer, namely, the content of interlayer Ca.

K_0 of coprecipitated C−S−H at Ca/Si of 0.8 is 40 GPa, lower than K_0 of 57 GPa for a single chain 11 Å tobermorite (Ca/Si = 0.83, non-cross-linked) in our recent HP-XRD study of different tobermorites.[61] The higher K_0 of single chain 11 Å tobermorite can be also explained by the influence of interlayer density. Although the C−S−H at Ca/Si of 0.8 shares a similar Ca/Si ratio with single chain 11 Å tobermorite (0.84 versus 0.83), the basal spacing of the two samples are different (12.76 versus 11.75 Å). The lower basal spacing but similar interlayer Ca content of single chain 11 Å tobermorite (higher interlayer density) result in the higher K_0 of this tobermorite. The positive correlation between interlayer density (namely, the *c*-axis incompressibility) and K_0 is also noticed in our recent HP-XRD study of tobermorite[61] and a computational study of Al-incorporated C−S−H.[34]

In the present study, we found a negative relationship between silicate polymerization and K_0 of C−S−H, whereas a recent study reported a positive correlation between macro-mechanical properties of C−S−H prisms with various Ca/Si ratios and their silicate chain lengths.[62] The contradiction may be explained by the influence of pore structure (not reported) in the macroscale measurement—the macroscale results are often affected by porosity and pore size distribution while HP-XRD studies investigate the mechanical properties of phases at a pore-free scale. Indeed, further investigation is needed to better understand the contradiction in the relationship between silicate polymerization and macromechanical properties of C−S−Hs. This influence of pore structure on the mechanical properties of C−S−H may also elucidate the contradicting negative Ca/Si-modulus correlation determined by nanoindentation.[63]

CONCLUSIONS

This study systematically investigates the correlation between the atomic structure and the nanomechanical properties of coprecipitated nanocrystalline C−S−H: the coordination environments of Ca and Si of the C−S−Hs were determined using XANES, and their nanomechanical properties were measured using HP-XRD. For the first time, C−S−H with comparable basal spacing (0.17 Å difference) at Ca/Si ratios of 0.8−1.5 was synthesized. The high-pH environment at low Ca/Si gives rise to a small quantity of octahedrally symmetric interlayer Ca while the interlayer Ca at higher Ca/Si ratios is more abundant but less symmetric (highly distorted). Silicate chains of C−S−H at low Ca/Si are highly polymerized while higher content of interlayer Ca at high Ca/Si leads to discontinuous silicate dimers. The incompressibility of C−S−H along the *a*- and *b*-axes is independent of Ca/Si ratio and silicate polymerization; that along the *c*-axis shows a positive correlation with the interlayer Ca content at a similar basal spacing. For the first time, the influences of basal spacing and Ca content on the nanomechanical properties of C−S−H are decoupled. The density of the interlayer essentially governs the incompressibility along the *c*-axis and the bulk modulus of C−S−H, which negatively correlates to silicate polymerization. The results have great implications for designing high-performance sustainable cement-based materials with a high volume of alkali-rich amorphous silicate (e.g., biomass ash, waste glass sludge, and agriculture waste ash) using bottom-up

https://dx.doi.org/10.1021/acssuschemeng.0c03230
ACS Sustainable Chem. Eng. 2020, 8, 12453−12461

approaches. The experimental results can provide reliable inputs of intrinsic mechanical properties of C−S−H for the multiscale modeling of cement/concrete properties. The findings are useful for validating the use of the Perdew−Burke−Ernzerhof generalized-gradient approximation in density functional theory studies of C−S−H[64] and C−S−H-based phases[65] and for parametrizing force fields (e.g., CSH-FF and Clay-FF) on the molecular dynamic studies of C−S−H.[66] For example, the Lennard-Jones potential of Ca−O, Ca−O_W, and Si−O_b and angular interaction within water molecules in molecular dynamic studies of C−S−H can be optimized.

■ ASSOCIATED CONTENT

Supporting Information

The Supporting Information is available free of charge at https://pubs.acs.org/doi/10.1021/acssuschemeng.0c03230.

Comparison between the present study and our previous study (PDF)

■ AUTHOR INFORMATION

Corresponding Author

Jiaqi Li − *Department of Civil and Environmental Engineering, University of California, Berkeley, California 94720, United States;* orcid.org/0000-0003-4863-6641; Email: Jiaqi.li@berkeley.edu

Authors

Wenxin Zhang − *Department of Civil and Environmental Engineering, University of California, Berkeley, California 94720, United States*

Paulo J. M. Monteiro − *Department of Civil and Environmental Engineering, University of California, Berkeley, California 94720, United States;* orcid.org/0000-0002-6866-1783

Complete contact information is available at: https://pubs.acs.org/10.1021/acssuschemeng.0c03230

Notes

The authors declare no competing financial interest.

■ ACKNOWLEDGMENTS

We thank Dr. Jinyuan Yan's support at ALS. David Gardner at UC Berkeley is thanked for his assistance of the experiments. This work is supported by the Republic of Singapore National Research Foundation through a grant to the Berkeley Education Alliance for Research in Singapore (BEARS) for the Singapore-Berkeley Building Efficiency and Sustainability in the Tropics (SinBerBEST) Program. This work is further funded by the US National Science Foundation under Division of Materials Research Ceramics Program, DMR-CER, Grant 1935604. The Advanced Light Source is supported by the Director, Office of Science, Office of Basic Energy Sciences, of the U.S. Department of Energy under Contract DE-AC02-05CH11231.

■ REFERENCES

(1) Miller, S. A.; Myers, R. J. Environmental Impacts of Alternative Cement Binders. *Environ. Sci. Technol.* **2020**, *54* (2), 677−686.

(2) Miller, S. A. Supplementary cementitious materials to mitigate greenhouse gas emissions from concrete: can there be too much of a good thing? *J. Cleaner Prod.* **2018**, *178*, 587−598.

(3) Diaz-Loya, I.; Juenger, M.; Seraj, S.; Minkara, R. Extending supplementary cementitious material resources: Reclaimed and remediated fly ash and natural pozzolans. *Cem. Concr. Compos.* **2019**, *101*, 44−51.

(4) Celik, K.; Meral, C.; Gursel, A. P.; Mehta, P. K.; Horvath, A.; Monteiro, P. J. M. Mechanical properties, durability, and life-cycle assessment of self-consolidating concrete mixtures made with blended portland cements containing fly ash and limestone powder. *Cem. Concr. Compos.* **2015**, *56*, 59−72.

(5) Provis, J. L. Alkali-activated materials. *Cem. Concr. Res.* **2018**, *114*, 40−48.

(6) Panda, B.; Ruan, S.; Unluer, C.; Tan, M. J. Investigation of the properties of alkali-activated slag mixes involving the use of nanoclay and nucleation seeds for 3D printing. *Composites, Part B* **2020**, *186*, 107826.

(7) Kastiukas, G.; Ruan, S.; Liang, S.; Zhou, X. Development of precast geopolymer concrete via oven and microwave radiation curing with an environmental assessment. *J. Cleaner Prod.* **2020**, *255*, 120290.

(8) Ma, B.; Lothenbach, B. Synthesis, characterization, and thermodynamic study of selected Na-based zeolites. *Cem. Concr. Res.* **2020**, *135*, 106111.

(9) Juenger, M. C. G.; Snellings, R.; Bernal, S. A. Supplementary cementitious materials: New sources, characterization, and performance insights. *Cem. Concr. Res.* **2019**, *122*, 257−273.

(10) Ma, B.; Fernandez-Martinez, A.; Grangeon, S.; Tournassat, C.; Findling, N.; Carrero, S.; Tisserand, D.; Bureau, S.; Elkaim, E.; Marini, C.; Aquilanti, G.; Koishi, A.; Marty, N. C. M.; Charlet, L. Selenite Uptake by Ca-Al LDH: A Description of Intercalated Anion Coordination Geometries. *Environ. Sci. Technol.* **2018**, *52* (3), 1624−1632.

(11) Arbi, K.; Palomo, A.; Fernandez-Jimenez, A. Alkali-activated blends of calcium aluminate cement and slag/diatomite. *Ceram. Int.* **2013**, *39* (8), 9237−9245.

(12) Celik, K.; Meral, C.; Mancio, M.; Mehta, P. K.; Monteiro, P. J. M. A comparative study of self-consolidating concretes incorporating high-volume natural pozzolan or high-volume fly ash. *Constr Build Mater.* **2014**, *67*, 14−19.

(13) Li, J.; Zhang, W.; Li, C.; Monteiro, P. J. M. Green concrete containing diatomaceous earth and limestone: Workability, mechanical properties, and life-cycle assessment. *J. Cleaner Prod.* **2019**, *223*, 662−679.

(14) Cheah, C. B.; Ramli, M. The implementation of wood waste ash as a partial cement replacement material in the production of structural grade concrete and mortar: An overview. *Resour Conserv Recy* **2011**, *55* (7), 669−685.

(15) Miller, S. A.; Cunningham, P. R.; Harvey, J. T. Rice-based ash in concrete: A review of past work and potential environmental sustainability. *Resour Conserv Recy* **2019**, *146*, 416−430.

(16) Lee, H.; Hanif, A.; Usman, M.; Sim, J.; Oh, H. Performance evaluation of concrete incorporating glass powder and glass sludge wastes as supplementary cementing material. *J. Cleaner Prod.* **2018**, *170*, 683−693.

(17) Uvegi, H.; Chaunsali, P.; Traynor, B.; Olivetti, E. Reactivity of industrial wastes as measured through ICP-OES: A case study on siliceous Indian biomass ash. *J. Am. Ceram. Soc.* **2019**, *102* (12), 7678−7688.

(18) Pimraksa, K.; Chindaprasirt, P. Lightweight bricks made of diatomaceous earth, lime and gypsum. *Ceram. Int.* **2009**, *35* (1), 471−478.

(19) Myers, R. J.; Bernal, S. A.; San Nicolas, R.; Provis, J. L. Generalized structural description of calcium−sodium aluminosilicate hydrate gels: the cross-linked substituted tobermorite model. *Langmuir* **2013**, *29* (17), 5294−5306.

(20) Richardson, I. G. Model structures for C-(A)-S-H (I). *Acta Crystallogr., Sect. B: Struct. Sci., Cryst. Eng. Mater.* **2014**, *70* (6), 903−923.

(21) Skinner, L. B.; Chae, S. R.; Benmore, C. J.; Wenk, H. R.; Monteiro, P. J. M. Nanostructure of Calcium Silicate Hydrates in Cements. *Phys. Rev. Lett.* **2010**, *104* (19), 195502.

(22) Jennings, H. M. Refinements to colloid model of C-S-H in cement: CM-II. *Cem. Concr. Res.* **2008**, *38* (3), 275−289.

(23) Bonaccorsi, E.; Merlino, S.; Kampf, A. R. The crystal structure of tobermorite 14 Å (plombierite), a C−S−H phase. *J. Am. Ceram. Soc.* **2005**, *88* (3), 505−512.
(24) Li, J.; Zhang, W.; Monteiro, P. J. Synchrotron X-ray Raman scattering shows the changes of the Ca environment in CSH exposed to high pressure. *Cem. Concr. Res.* **2020**, *132*, 106066.
(25) Dolado, J. S.; Griebel, M.; Hamaekers, J. A molecular dynamic study of cementitious calcium silicate hydrate (C-S-H) gels. *J. Am. Ceram. Soc.* **2007**, *90* (12), 3938−3942.
(26) Hou, D. S.; Li, T. Influence of aluminates on the structure and dynamics of water and ions in the nanometer channel of calcium silicate hydrate (C-S-H) gel. *Phys. Chem. Chem. Phys.* **2018**, *20* (4), 2373−2387.
(27) Ulm, F. J.; Vandamme, M.; Jennings, H. M.; Vanzo, J.; Bentivegna, M.; Krakowiak, K. J.; Constantinides, G.; Bobko, C. P.; Van Vliet, K. J. Does microstructure matter for statistical nano-indentation techniques? *Cem. Concr. Compos.* **2010**, *32* (1), 92−99.
(28) Trtik, P.; Munch, B.; Lura, P. A critical examination of statistical nanoindentation on model materials and hardened cement pastes based on virtual experiments. *Cem. Concr. Compos.* **2009**, *31* (10), 705−714.
(29) Geng, G.; Myers, R. J.; Li, J.; Maboudian, R.; Carraro, C.; Shapiro, D. A.; Monteiro, P. J. Aluminum-induced dreierketten chain cross-links increase the mechanical properties of nanocrystalline calcium aluminosilicate hydrate. *Sci. Rep.* **2017**, *7*, 44032.
(30) Geng, G.; Myers, R. J.; Qomi, M. J. A.; Monteiro, P. J. M. Densification of the interlayer spacing governs the nanomechanical properties of calcium-silicate-hydrate. *Sci. Rep.* **2017**, *7*, 10986.
(31) L'Hôpital, E.; Lothenbach, B.; Kulik, D.; Scrivener, K. Influence of calcium to silica ratio on aluminium uptake in calcium silicate hydrate. *Cem. Concr. Res.* **2016**, *85*, 111−121.
(32) Li, J.; Yu, Q. J.; Huang, H. L.; Yin, S. H. Effects of Ca/Si Ratio, Aluminum and Magnesium on the Carbonation Behavior of Calcium Silicate Hydrate. *Materials* **2019**, *12* (8), 1268.
(33) Dolado, J. S.; Griebel, M.; Hamaekers, J.; Heber, F. The nano-branched structure of cementitious calcium-silicate-hydrate gel. *J. Mater. Chem.* **2011**, *21* (12), 4445−4449.
(34) Yang, J.; Hou, D. S.; Ding, Q. J. Structure, Dynamics, and Mechanical Properties of Cross-Linked Calcium Aluminosilicate Hydrate: A Molecular Dynamics Study. *ACS Sustainable Chem. Eng.* **2018**, *6* (7), 9403−9417.
(35) Bae, S.; Taylor, R.; Hernandez-Cruz, D.; Yoon, S.; Kilcoyne, D.; Monteiro, P. J. M. Soft X-ray Spectromicroscopic Investigation of Synthetic C-S-H and C3S Hydration Products. *J. Am. Ceram. Soc.* **2015**, *98* (9), 2914−2920.
(36) L'Hôpital, E.; Lothenbach, B.; Scrivener, K.; Kulik, D. Alkali uptake in calcium alumina silicate hydrate (C-A-S-H). *Cem. Concr. Res.* **2016**, *85*, 122−136.
(37) Orozco, C. A.; Chun, B. W.; Geng, G.; Emwas, A. H.; Monteiro, P. J. Characterization of the bonds developed between calcium silicate hydrate and polycarboxylate-based superplasticizers with silyl functionalities. *Langmuir* **2017**, *33* (14), 3404−3412.
(38) Chiang, W.-S.; Fratini, E.; Baglioni, P.; Liu, D.; Chen, S.-H. Microstructure determination of calcium-silicate-hydrate globules by small-angle neutron scattering. *J. Phys. Chem. C* **2012**, *116* (8), 5055−5061.
(39) Moon, J. H.; Oh, J. E.; Balonis, M.; Glasser, F. P.; Clark, S. M.; Monteiro, P. J. M. Pressure induced reactions amongst calcium aluminate hydrate phases. *Cem. Concr. Res.* **2011**, *41* (6), 571−578.
(40) Merlino, S.; Bonaccorsi, E.; Armbruster, T. The real structure of tobermorite 11 angstrom: normal and anomalous forms, OD character and polytypic modifications. *Eur. J. Mineral.* **2001**, *13* (3), 577−590.
(41) Naftel, S. J.; Sham, T. K.; Yiu, Y. M.; Yates, B. W. Calcium L-edge XANES study of some calcium compounds. *J. Synchrotron Radiat.* **2001**, *8*, 255−257.
(42) Li, J.; Geng, G.; Zhang, W.; Yu, Y. S.; Shapiro, D. A.; Monteiro, P. J. M. The Hydration of beta- and alpha(H)′-Dicalcium Silicates: An X-ray Spectromicroscopic Study. *ACS Sustainable Chem. Eng.* **2019**, *7* (2), 2316−2326.
(43) Geng, G.; Taylor, R.; Bae, S.; Hernandez-Cruz, D.; Kilcoyne, D. A.; Emwas, A. H.; Monteiro, P. J. M. Atomic and nano-scale characterization of a 50-year-old hydrated C3S paste. *Cem. Concr. Res.* **2015**, *77*, 36−46.
(44) Ko, J. P. X-ray Absorption Near-edge Structure (XANES) of Calcium L3,2 Edges of Various Calcium Compounds and X-ray Excited Optical Luminescence (XEOL) Studies of Luminescent Calcium Compounds. *X-Ray Absorption Fine Structure–XAFS* **2006**, *13* (882), 538−540.
(45) Geng, G.; Li, J.; Yu, Y.-S.; Shapiro, D. A.; Kilcoyne, D. A.; Monteiro, P. J. Nanometer-Resolved Spectroscopic Study Reveals the Conversion Mechanism of CaO·Al2O3·10H2O to 2CaO·Al2O3·8H2O and 3CaO·Al2O3·6H2O at an Elevated Temperature. *Cryst. Growth Des.* **2017**, *17* (8), 4246−4253.
(46) Manzano, H.; Dolado, J. S.; Guerrero, A.; Ayuela, A. Mechanical properties of crystalline calcium-silicate-hydrates: comparison with cementitious C-S-H gels. *Phys. Status Solidi A* **2007**, *204* (6), 1775−1780.
(47) Li, J.; Geng, G.; Myers, R.; Yu, Y. S.; Shapiro, D.; Carraro, C.; Maboudian, R.; Monteiro, P. J. M. The chemistry and structure of calcium (alumino) silicate hydrate: A study by XANES, ptychographic imaging, and wide- and small-angle scattering. *Cem. Concr. Res.* **2019**, *115*, 367−378.
(48) Gartner, E.; Maruyama, I.; Chen, J. A new model for the C-S-H phase formed during the hydration of Portland cements. *Cem. Concr. Res.* **2017**, *97*, 95−106.
(49) Kumar, A.; Walder, B. J.; Mohamed, A. K.; Hofstetter, A.; Srinivasan, B.; Rossini, A. J.; Scrivener, K.; Emsley, L.; Bowen, P. The Atomic-Level Structure of Cementitious Calcium Silicate Hydrate. *J. Phys. Chem. C* **2017**, *121* (32), 17188−17196.
(50) Cabaret, D.; Le Grand, M.; Ramos, A.; Flank, A. M.; Rossano, S.; Galoisy, L.; Calas, G.; Ghaleb, D. Medium range structure of borosilicate glasses from Si K-edge XANES: a combined approach based on multiple scattering and molecular dynamics calculations. *J. Non-Cryst. Solids* **2001**, *289* (1−3), 1−8.
(51) Ma, B.; Fernandez-Martinez, A.; Made, B.; Findling, N.; Markelova, E.; Salas-Colera, E.; Maffeis, T. G. G.; Lewis, A. R.; Tisserand, D.; Bureau, S.; Charlet, L. XANES-Based Determination of Redox Potentials Imposed by Steel Corrosion Products in Cement-Based Media. *Environ. Sci. Technol.* **2018**, *52* (20), 11931−11940.
(52) Li, D.; Bancroft, G. M.; Fleet, M. E.; Feng, X. H. Silicon K-Edge Xanes Spectra of Silicate Minerals. *Phys. Chem. Miner.* **1995**, *22* (2), 115−122.
(53) Henderson, G. S. A Si K-Edge Exafs/Xanes Study of Sodium-Silicate Glasses. *J. Non-Cryst. Solids* **1995**, *183* (1−2), 43−50.
(54) Henderson, G. S.; Fleet, M. E. The structure of titanium silicate glasses investigated by Si K-edge X-ray absorption spectroscopy. *J. Non-Cryst. Solids* **1997**, *211* (3), 214−221.
(55) Bianconi, A.; Dellariccia, M.; Durham, P. J.; Pendry, J. B. Multiple-Scattering Resonances and Structural Effects in the X-Ray-Absorption near-Edge Spectra of Fe-Ii and Fe-Iii Hexacyanide Complexes. *Phys. Rev. B: Condens. Matter Mater. Phys.* **1982**, *26* (12), 6502−6508.
(56) Hay, R.; Li, J.; Celik, K. Influencing factors on micromechanical properties of calcium (alumino) silicate hydrate C-(A-)S-H under nanoindentation experiment. *Cem. Concr. Res.* **2020**, *134*, 106088.
(57) Hunnicutt, W.; Struble, L.; Mondal, P. Effect of synthesis procedure on carbonation of calcium-silicate-hydrate. *J. Am. Ceram. Soc.* **2017**, *100* (8), 3736−3745.
(58) Geng, G.; Li, J.; Zhou, Y.; Liu, L.; Yan, J.; Kunz, M.; Monteiro, P. J. M. A high-pressure X-ray diffraction study of the crystalline phases in calcium aluminate cement paste. *Cem. Concr. Res.* **2018**, *108*, 38−45.
(59) Geng, G.; Vasin, R. N.; Li, J.; Qomi, M. J. A.; Yan, J.; Wenk, H. R.; Monteiro, P. J. M. Preferred orientation of calcium aluminosilicate hydrate induced by confined compression. *Cem. Concr. Res.* **2018**, *113*, 186−196.

https://dx.doi.org/10.1021/acssuschemeng.0c03230
ACS Sustainable Chem. Eng. 2020, 8, 12453−12461

(60) Li, J.; Zhang, W.; Monteiro, P. J. Mechanical properties of struvite-K: A high-pressure X-ray diffraction study. *Cem. Concr. Res.* **2020**, *136*, 106171.
(61) Li, J.; Zhang, W.; Garbev, K.; Beuchle, G.; Monteiro, P. J. Influences of cross-linking and Al incorporation on the intrinsic mechanical properties of tobermorite. *Cem. Concr. Res.* **2020**, *136*, 106170.
(62) Kunther, W.; Ferreiro, S.; Skibsted, J. Influence of the Ca/Si ratio on the compressive strength of cementitious calcium-silicate-hydrate binders. *J. Mater. Chem. A* **2017**, *5* (33), 17401−17412.
(63) Abdolhosseini Qomi, M.J.; Krakowiak, K.J.; Bauchy, M.; Stewart, K.L.; Shahsavari, R.; Jagannathan, D.; Brommer, D.B.; Baronnet, A.; Buehler, M.J.; Yip, S.; Ulm, F.-J; Van Vliet, K.J.; Pellenq, R.J.-M. Combinatorial molecular optimization of cement hydrates. *Nat. Commun.* **2014**, *5*, 1−10.
(64) Ozcelik, V. O.; White, C. E. Nanoscale Charge-Balancing Mechanism in Alkali-Substituted Calcium-Silicate-Hydrate Gels. *J. Phys. Chem. Lett.* **2016**, *7* (24), 5266−5272.
(65) Ozcelik, V. O.; Garg, N.; White, C. E. Symmetry-Induced Stability in Alkali-Doped Calcium Silicate Hydrate. *J. Phys. Chem. C* **2019**, *123* (22), 14081−14088.
(66) Manzano, H.; Durgun, E.; Lopez-Arbeloa, I.; Grossman, J. C. Insight on Tricalcium Silicate Hydration and Dissolution Mechanism from Molecular Simulations. *ACS Appl. Mater. Interfaces* **2015**, *7* (27), 14726−14733.

https://dx.doi.org/10.1021/acssuschemeng.0c03230
ACS Sustainable Chem. Eng. 2020, 8, 12453−12461